Experimental Results on Stability of Cylindrical Shells Under Combined Bending and Torsion

Victoria Ding[1], Shahab Torabian[2], Sandor Adany[3], Xiang Yun[4],
Anil Pervizaj[5], Andrew T. Myers[6], Benjamin W. Schafer[7]

[1]Ph.D. Candidate, Johns Hopkins University, Baltimore, MD, USA (corresponding author). Email: vding1@jhu.edu

[2]Associate Research Scientist, Johns Hopkins University, Baltimore, MD, USA. Email: torabian@jhu.edu

[3]Visiting Faculty Scholar, Johns Hopkins University, Baltimore, MD, USA. Email: asandor2@jhu.edu

[4]Lecturer, University of Sheffield, Sheffield, UK. Email: x.yun@sheffield.ac.uk

[5]Lead Engineer - Tower Technology, Vestas, Aarhus, Denmark. Email: anpij@vestas.com

[6]Associate Professor, Northeastern University, Boston, MA, USA. Email: an.myers@northeastern.edu

[7]Professor, Johns Hopkins University, Baltimore, MD, USA. Email: schafer@jhu.edu

Abstract

Modern wind turbines are often supported by tubular steel towers, which are made from globally conical, locally cylindrical, shells with relatively large diameter-to-thickness ratios – roughly between 100 and 300 – to use the tower material as efficiently as possible. Wind turbine towers face complex loading resulting from both environmental and operational load cases and are sensitive to geometrical imperfections that inevitably arise during the fabrication process. While bending often controls at the base of turbine towers, the upper sections are controlled by combined bending and torsion. Though extensive studies have been conducted on the stability and design of cylinders subjected to isolated actions, investigations into the structural response of thin-walled cylinders under combined actions, such as bending and torsion, remain limited. To address this knowledge gap, an experimental program was carried out to study the structural behavior of thin-walled steel cylinders under combined bending and torsion. A total of 48 cylinders were tested

with varying diameter-to-thickness ratios and torsion-to-moment ratios found in wind turbine towers. To gain insight into the imperfection sensitivity of these tests, a laser scanner was used to measure geometric imperfections of each specimen before testing. The test setup, instrumentation, loading procedures and structural response of the cylinders, including ultimate resistances, load-deformation characteristics and failure modes are reported. The primary objective of this study is to provide benchmark test data for the validation of numerical models and the development of advanced design methodologies, such as Reference Resistance Design (RRD), for cylindrical shells under combined bending and torsion. Future work will involve formulating guidelines for using laser-scanned data to evaluate geometric imperfections, developing laboratory-scale and full-scale wind turbine tower finite element models, and ultimately providing improved design guidance on combined bending and torsion.

Introduction

The stability of thin shells is a longstanding problem in structural design. Today, one application for thin shells is the use of thin steel cylindrical tubes as supporting towers for wind turbines. While bending often controls at the base of turbine towers, the upper sections are controlled by combined bending and torsion. Designing towers with large diameter-to-thickness (D/t) ratios is a strategic approach to reduce material usage and create structurally efficient towers. Excess steel material increases the carbon footprint of the tower, so sustainability goals push towards the most efficient possible use of the material. However, nothing is more wasteful than a structural tower failure, so structural efficiency must be balanced by structural reliability. Further complicating the problem are some of the specifics of wind turbine tower design, including the balance between fatigue and stability-driven failures, the relatively complex loading actions that can create unique bending and torsion demands on the same segment of the tower, and additional considerations, such as transportation and assembly limitations (Veritas 2002).

Existing research on slender cylindrical steel shells has focused primarily on isolated actions. Historically, this has included foundational stability work for isolated compression (e.g., Timoshenko 1961), flexure (e.g., Seide and Weingarten 1961), and torsion (Donnell 1935) as well as extensive physical testing, e.g. as recently summarized for compression of metallic shells by (Sadowski et al. 2023) or in the recent tests on new potential solutions for wind turbine support towers tested in compression (Ren et al. 2023) or flexure (Jay et al. 2016). For combined actions the work of Teng and Rotter (1989) and later Sadowski and Rotter (2012) developed and established the potential for numerical solutions for steel shells, while Winterstetter and Schmidt (2002) provide the most comprehensive summary of experimental performance. Winterstetter and Schmidt note a profound need for additional work under axial and shear forces, and provided testing for stocky cylinders under this condition. Recently Ren et al. (2022) investigated a stiffened shell under combined compression, bending and torsion.

Design codes and standards do cover the design of cylindrical shells subjected to combined actions. For example, Eurocode 1993-1-6 (ECCS 2021) provides an interaction equation for cylinders under combined actions, encompassing the axial, shear, and hoop stresses that develop in the cylinders. Eurocode's expressions are of primary interest and are fully detailed in comparison to the experimental results discussed later in this paper. In addition, the AISC Specification for the Design of Steel Hollow Structural Sections (2000) also provides guidance on combined bending and torsion. The AISC Specification presents two interaction equations for load combinations involving both normal and shear stresses, based on the work of Felton and Dobbs (1967) and Schilling (1965).

Another complication of thin shells is their high imperfection sensitivity, which means accurately predicting their structural response is difficult. Any manufactured structure will inevitably have imperfections, and the reduced failure loads of shells are largely correlated with these imperfections. Standards of practice for a variety of structural engineering applications that utilize thin shells have been successfully established and utilized by engineers, see (ECCS 2021) for reference, and discussion in (Rotter and Schmidt 2014). However, each time engineers explore new domains for thin shells, they are confronted with the imperfection sensitivity in the structural response of these members, necessitating the development or updating adequate design procedures. Studies on combined bending and torsion of thin cylindrical shells, or how their imperfection sensitivity affects this load case, are scarce within the widely available literature. Design of the upper segment of wind turbine support towers is often controlled by combined bending and torsion, and minimal benchmark test data exists for slender steel cylinders in this condition.

To address this substantial knowledge gap, an experimental study on the stability of cylinders with large diameter-to-thickness ratios under combined bending and torsion has been conducted and is presented in this paper. A total of 48 cylinders, with diameter-to-thickness ratios ranging from 127 to 320, were tested under varying bending and torsion combinations seen in wind turbine towers. Given the sensitivity of the stability of thin-walled cylinders to geometric imperfections, 3D laser scanning was used to precisely quantify the geometric imperfections of each test specimen prior to testing. The experimental setup for the combined bending and torsion tests, alongside the instrumentation, loading procedures and key test results, including ultimate resistances, load-deformation characteristics and failure modes, are reported herein. The primary objective of this study is to provide benchmark test data for the validation of numerical models and the development of advanced design methodologies, such as Reference Resistance Design (RRD) (Wang et al. 2020), for cylindrical shells under combined bending and torsion. Future work will involve creating guidelines on how to use laser-scanned data to classify imperfections, as well as establishing high-fidelity finite element models capable of capturing the buckling strength and failure mode of thin-walled cylinders under different loading scenarios, and developing reliable and efficient design approaches for such structural elements.

Steel Monopole Wind Turbine Towers

Steel wind turbine towers must be certified before use. Certification bodies, such as DNV, provide certification and detailed design information for components of wind turbines, including support towers (Veritas 2002). Here we focus only on stability and ignore fatigue and other details required to fully design and certify a tower. Discussion is limited to three major issues; (1) the critical loading actions experienced by wind turbine towers, (2) the typical slenderness of towers, and (3) the tube geometries that are used for laboratory scale testing.

Critical loading actions

Fig. 1 illustrates the various loads that wind turbines encounter. A typical wind turbine tower under wind load functions like a cantilever with some unique features at a particular time. Fig. 1 shows time histories of bending moment and torsion at the top of a tower when the wind turbine is operating and subjected to an extreme coherent wind gust with directional change. Under these conditions, the interaction of bending moment, torsion, shear, and axial force along the tower is significant. The blades can yaw so that they are in line with the wind, but that does not happen instantly. This lack of alignment creates torsion. Wind on the blades and the tower result in large moment at the base, which controls design of the bottom portion of the tower. To better predict demand, load calculations were done in OpenFAST (Jonkman 2005), which is an open-source wind turbine simulation tool. When considering actual tower designs (Jonkman 2009, Gaertner 2020), one can observe that the combination of torsion and moment controls the design of the top portion of the tower.

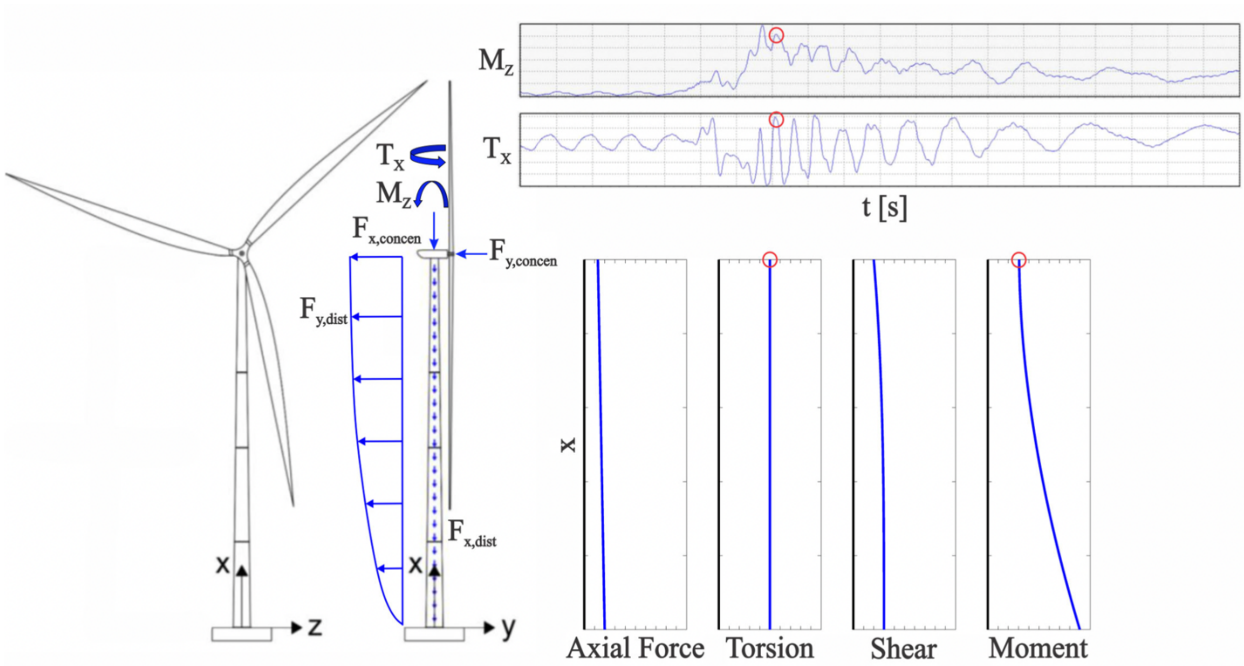

Fig. 1. Instantaneous distributions of axial force, torsion, shear, and moment

<u>*Slenderness of Wind Turbine Towers*</u>

Fig. 2 and 3 provide geometry for typical onshore turbine towers in use today by Vestas. Fig. 2 provides a scaled drawing of a typical steel monopole wind turbine tower. Turbine towers are slender, with many over 100 meters tall and base diameters generally at least 4 meters wide. Wind turbine towers are not perfectly cylindrical. Towers are built up from cans welded together, and as height increases, the can diameter decreases (and thickness changes), providing an overall taper.

Typical cans are represented between dashed lines and are welded together to form segments shown between solid lines in Fig. 2. Flanges are used for connecting segments and provide some strength against ovalization. Fig. 3 shows data on 45 in-service onshore wind turbine towers from Vestas. In Fig. 3a, each line represents diameter-to-thickness ratios, or D/t, of one turbine tower along its normalized height. D/t ratios are low (i.e., the tower is "stockier") at the base of the tower to resist high moment demand. Moment demand decreases as elevation increases, so D/t ratios increase (i.e., the cans become more slender) as height increases, excepting the top most sections which are again stockier (low D/t) to accommodate localized demands. The mean D/t ratio of these 45 towers is 180. Fig. 3b provides a histogram of tower heights. The mean height in the sampled towers is 123 m with a coefficient of variation (CV) of 0.19. Fig. 3c provides a histogram of height-to-base-diameter ratios. The ratio for the height of a tower to its base diameter is typically around 28. Finally, Fig. 3d provides a histogram of the maximum D/t of each tower. The mean of the maximum D/t ratio of each tower is 256, and the maximum observed across all 45 towers is 300.

144
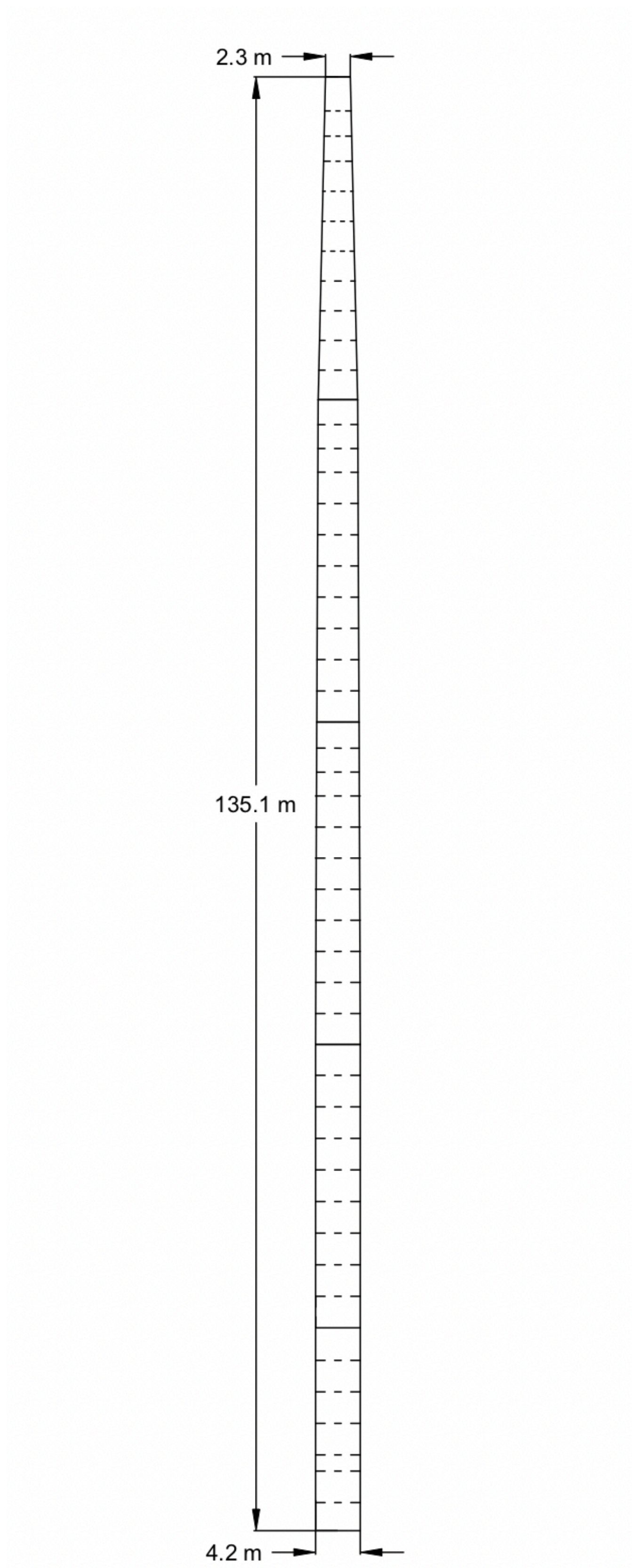

145 **Fig. 2.** Scaled drawing of a typical onshore wind turbine tower

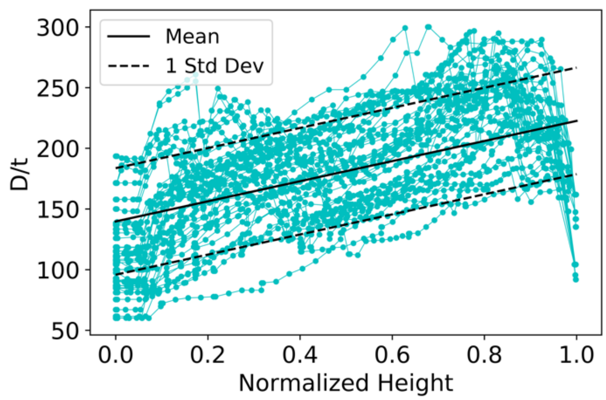

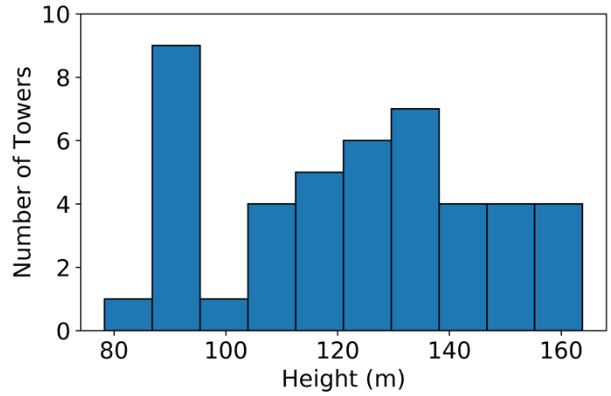

(a) D/t variation across tower height

(b) Histogram of tower heights

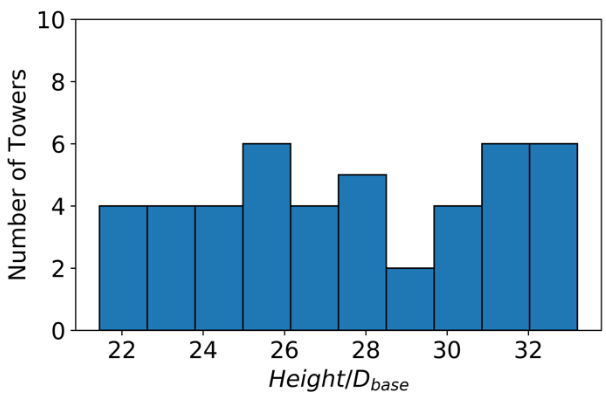

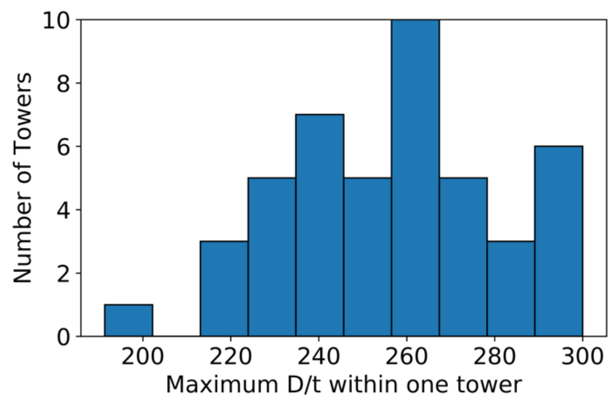

(c) Histogram of height-to-base diameter ratios

(d) Histogram of each tower's maximum D/t

Fig. 3. Wind turbine tower statistics

Tube geometries for laboratory scale testing

In accordance with current practice for wind turbine towers and with an eye towards potentially using even more slender sections, we selected steel cylinders with D/t from 127 to 320. Conveniently, and somewhat remarkably, Nordfab Ducting fabricates cylindrical steel members within this range at a scale suitable for laboratory-scale testing. Though D/t matches, D obviously is smaller in the lab; based on an average tower D of 3m the laboratory scale ranges from 30:1 at the smallest tube studied to 12:1 at the largest tube (see next section for complete dimensions).

Experimental Tests on Cylindrical Shells Under Combined Bending and Torsion

Experiments on cylindrical shells under combined bending and torsion were conducted in the Thin-walled Structures Laboratory at Johns Hopkins University. Table 1 provides dimensions and loading configurations for each tube. There are 48 tubes in total; 4 different sized tubes and 12 of each size. Each size has 4 different torque-to-moment (T/M) loading ratios. In actual tower designs (Jonkman 2009, Gaertner 2020), T/M is typically between 0 and 1. T/M = 0 means bending only and T/M = 1 means the amount of torque and moment are equal.

Table 1. Nominal dimensions and geometry for experiments

Nominal Size (mm)	D[a] (mm)	t (mm)	L (mm)	D/t	L/D	Outrigger (mm)	Moment arm (mm)	T/M	Number of Specimens
100	100	0.79	300	127	3	149	449	1	3
100	100	0.79	300	127	3	149	449	0.66	3
100	100	0.79	300	127	3	149	449	0.33	3
100	100	0.79	300	127	3	149	449	0	3
150	151	0.79	453	191	3	149	602	1	3
150	151	0.79	453	191	3	149	602	0.66	3
150	151	0.79	453	191	3	149	602	0.33	3
150	151	0.79	453	191	3	149	602	0	3
200	202	0.79	606	256	3	149	755	1	3
200	202	0.79	606	256	3	149	755	0.66	3
200	202	0.79	606	256	3	149	755	0.33	3
200	202	0.79	606	256	3	149	755	0	3
250	253	0.79	759	320	3	149	908	1	3
250	253	0.79	759	320	3	149	908	0.66	3
250	253	0.79	759	320	3	149	908	0.33	3
250	253	0.79	759	320	3	149	908	0	3

[a]D is outer diameter

Laser Scanning

All tubes were laser scanned to determine their precise initial geometry prior to being tested. Fig. 4 provides a photo of a 250mm diameter tube in the lab's laser scanning rig (Zhao et al. 2015). The laser scanner is a line laser and the model is Keyence LJ-V7300. Accuracy ranges from 0.1mm to 0.3mm depending on the distance from the specimen to the laser.

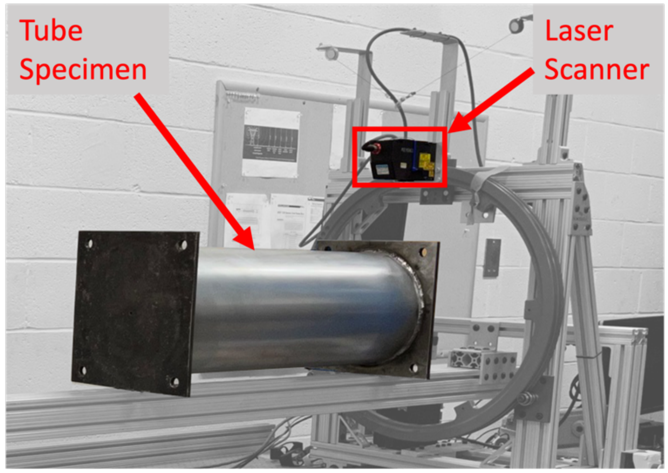

Fig. 4. Laser scanning rig with a 250mm diameter tube

Fig. 5 provides an example of a full scan point cloud of a 250mm tube after post-processing, and Fig. 6 provides a representation of the scan showing the radial deviation as a contours from the unwrapped tube with the seam weld located at 0 radians.

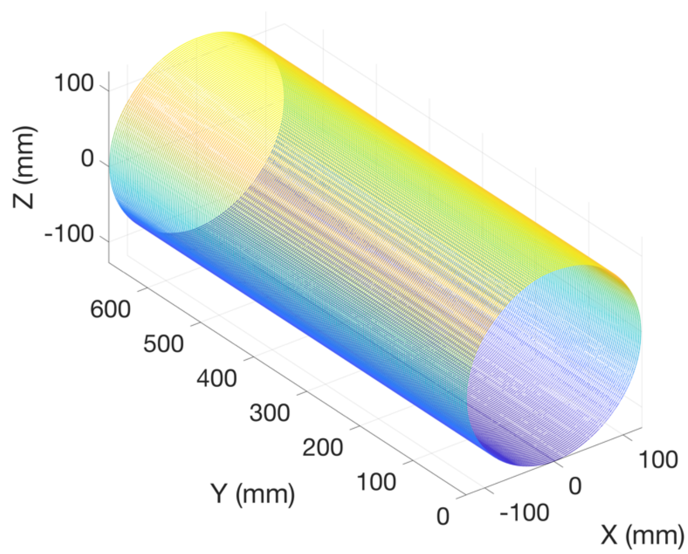

Fig. 5. Post-processed scanned data of a 250mm tube

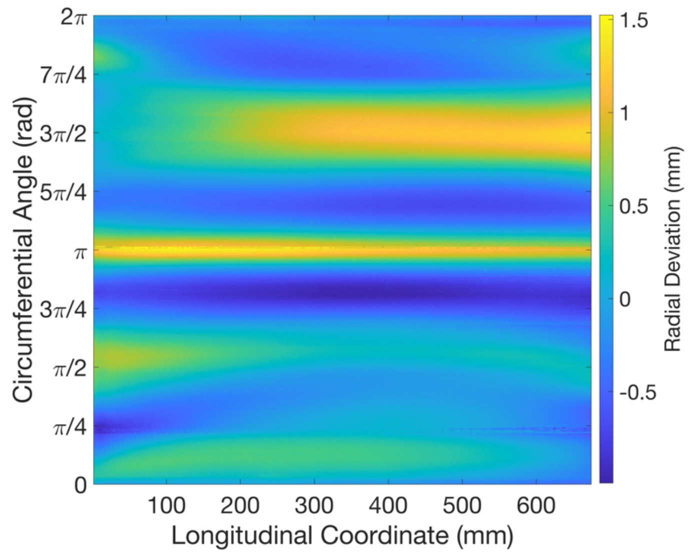

Fig. 6. Radial deviations of a 250mm tube

To predict design strength, Eurocode (ECCS 2021) uses fabrication quality classes (QC), which reflect the severity of geometric imperfections in a specimen. Class A is excellent quality, class B is high quality, and class C is normal quality. Eurocode's guidelines for assigning QC are for physical measurements. Currently there are no guidelines for how to assign QC with laser scanned imperfections. Table 2 provides the QCs of each tube using the laser scanned data at the 95th percentile, 99th percentile, and the worst data. Assigning QC using the worst of the worst data is one possible method for physical measurements, but doing the same for laser scanned data leads to overly conservative strength predictions because laser scans record much more data than physical measurements. If the worst laser scanned data is used to assign QC in this study, several tubes are class C, and the rest are worse than C. However, all tubes fall within classes A-C when comparing the experimental results to their predicted Eurocode strengths. The focus of the work of this paper is the experimental results themselves – future work will address how laser scanned data can best be utilized in predicting design strength.

Table 2: Quality class of each tube specimen

	Quality Class				Quality Class		
Specimen	95th %ile	99th %ile	Worst	Specimen	95th %ile	99th %ile	Worst
250mm-1[a]	B	C	WTC	150mm-1	C	C	WTC
250mm-2	C	C	WTC	150mm-2	B	C	WTC
250mm-3	B	C	C	150mm-3	A	B	WTC
250mm-4	C	C	WTC	150mm-4	A	A	WTC
250mm-5	B	C	WTC	150mm-5	A	B	WTC
250mm-6	C	C	WTC	150mm-6[a]	C	C	WTC
250mm-7	WTC	WTC	WTC	150mm-7	A	B	WTC
250mm-8	C	C	WTC	150mm-8	A	B	WTC
250mm-9	C	C	WTC	150mm-9	A	B	WTC
250mm-10	C	WTC	WTC	150mm-10	B	C	WTC
250mm-11	C	C	WTC	150mm-11	A	B	WTC
250mm-12	C	WTC	WTC	150mm-12	B	B	WTC
200mm-1	C	C	WTC	100mm-1	C	C	WTC
200mm-2	WTC	WTC	WTC	100mm-2	B	B	WTC
200mm-3	C	C	WTC	100mm-3	C	C	WTC
200mm-4	B	C	C	100mm-4	A	B	WTC
200mm-5	B	B	WTC	100mm-5	C	WTC	WTC
200mm-6	C	WTC	WTC	100mm-6	C	C	WTC
200mm-7	C	C	WTC	100mm-7	WTC	WTC	WTC
200mm-8	B	C	WTC	100mm-8	B	B	WTC
200mm-9	B	C	WTC	100mm-9	C	C	WTC
200mm-10	C	C	WTC	100mm-10	C	C	WTC
200mm-11	C	C	WTC	100mm-11	B	WTC	WTC
200mm-12	WTC	WTC	WTC	100mm-12	B	B	WTC

[a]These tubes were accidentally dented before testing

Tensile Tests

Material properties were determined from tensile tests conducted to ASTM-E8 (2012). Coupon specimens were extracted from the cylinders in the longitudinal and transverse directions, including coupons that cross the longitudinal seam weld from fabrication, as shown in Fig. 7.

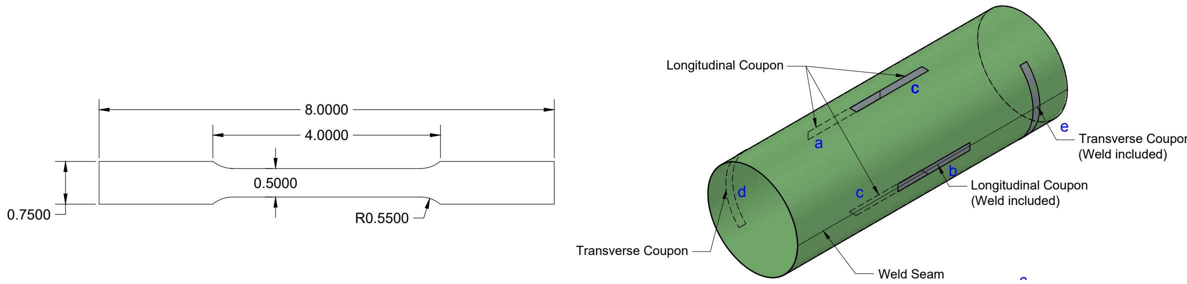

Fig. 7. Tensile coupon dimensions and locations from tube

Tensile tests were conducted using an MTS Criterion Model 43 testing machine and the MTS software TW Elite. Loading rate was 0.0254mm/sec (0.001 in/sec). An extensometer was attached to each coupon to measure elongation and no strain gauges were used. The elastic modulus of various steel grades was found to be consistently around 210 MPa (30500 ksi) in Yun and Gardner (2017), and this value is assumed for the purposes of this study. Tensile stress-strain response of longitudinal coupons without welds is provided in Fig. 8. These coupons have consistent yield strengths and behavior for a given tube size.

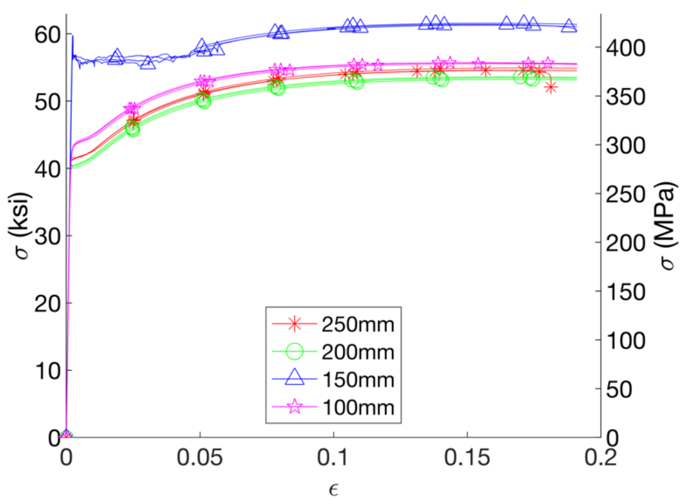

Figure 8. Stress-strain curves of longitudinal coupons without welds for each tube diameter

Measured thickness, calculated yield stress (F_y) based on the 0.2% offset, ultimate stress (F_u), and elongation at fracture for all coupons are summarized in Table 3. Note, different tube sizes are fabricated from different initial coils and thus have different yield strengths; however, all specimens for a given size are fabricated from the same coil. The F_y of longitudinal coupons without welds is used in modeling and calculations. Elongation at failure is around 20% for all coupons except for the 100mm coupon that was cut transverse across the weld. This was due to a dent in the gage section of that coupon.

Table 3. Tensile Test Results

Tube Size	Coupon Type	Thickness (mm)	F_y (MPa)	F_u (MPa)	Elongation (%)	Number of coupons
100mm	**Longitudinal**	**0.72**	**301**	384	19.7%	3
	Long. along weld	0.73	291	374	18.3%	1
	Transverse	0.72	277	383	18.5%	1
	Trans. across weld	0.73	248	374	10.8%	1
150mm	**Longitudinal**	**0.72**	**390**	424	18.7%	3
	Long. along weld	0.73	397	434	18.1%	1
	Transverse	0.73	365	420	21.2%	1
	Trans. across weld	0.72	350	424	18.4%	1
200mm	**Longitudinal**	**0.73**	**278**	368	20.6%	3
	Long. along weld	0.75	294	381	18.4%	1
	Transverse	0.73	265	361	23.9%	1
	Trans. across weld	0.74	263	370	19.6%	1
250mm	**Longitudinal**	**0.73**	**287**	377	21.7%	3
	Long. along weld	0.78	306	393	21.0%	1
	Transverse	0.73	296	385	23.7%	1
	Trans. across weld	0.73	277	377	21.0%	1

<u>Experimental Test Setup</u>

Fig. 9 shows the test rig for the cylindrical shells under combined bending and torsion with a 250mm diameter tube loaded with T/M = 0.33 (Ding 2023).

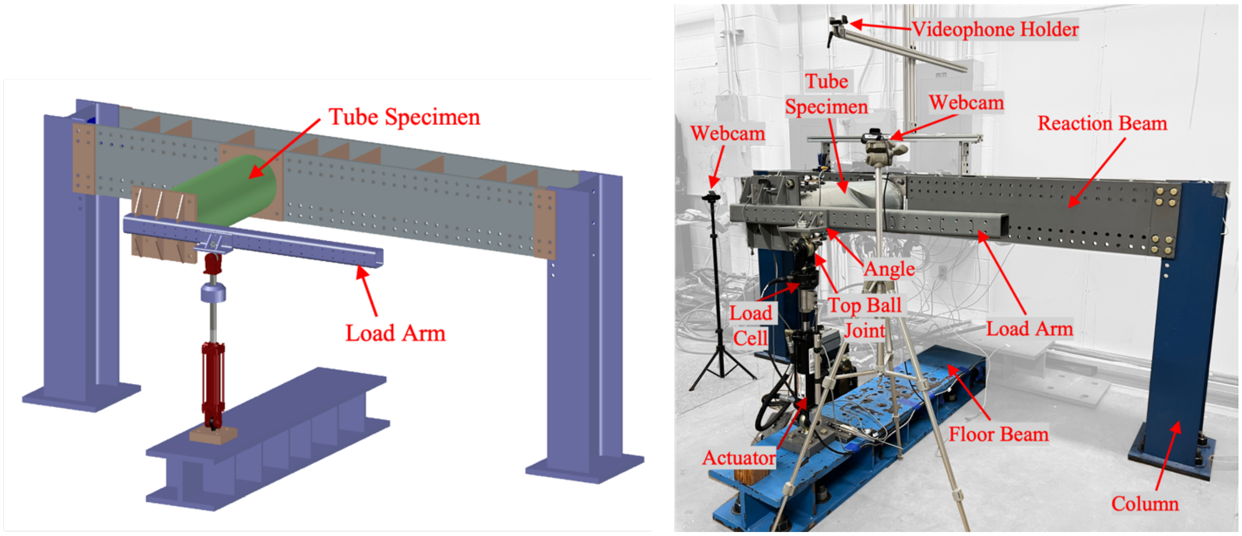

(a) Drawing of test rig (b) Photo of test rig

Fig. 9. Combined bending and torsion test rig with a 250mm tube loaded with T/M=0.33

The tubes were manufactured by Nordfab by rolling a thin sheet into a cylinder and then welding the seam. Nordfab cut the tubes to the specified length and shipped them to FABCO, a precision machine shop, which welded square plates to both ends so the specimens could be attached to the testing rig. The load arm is stiff and introduces eccentricity, providing torsion in addition to bending. The load is applied upward against gravity on the load arm so that self-weight can be eliminated. To apply different T/M ratios, the tube is installed at different locations along the reaction beam while the actuator stays in place. To accommodate different tube lengths, the actuator can be placed at different locations along the floor beam. Note, due to the end plate to accommodate the load arm the distance from the free end of the tube to where the load is applied is 149mm (6 in.) for all tests. The actuator is a 20.7MPa (3000 psi) hydraulic cylinder with a load capacity of 65500 N (14,720 pounds). A load cell and position transducer (PT) are attached to the actuator to record changes in load and control the crosshead displacement. Both ends of the actuator have clevis mounts attached to ball joints. The bottom ball joint is threaded into a plate which is bolted to the floor beam. The top ball joint is bolted to an angle which is bolted to the load arm. Three videos were recorded at different positions for each tube to capture the failure response during testing. Fig. 10 provides the coordinate system, PT locations, and angle definitions. Six PTs are attached to the end plate. These PTs are used to calculate displacement and angle changes of the end plate during loading. The PTs are “spring loaded” and can stroke in or out. PT1 to PT4 are attached to bolts that connect the load arm to the end plate and can stroke up to 28 mm (1.125 in.). PT5 and PT6 are placed on the floor and attached to heavy steel plates to prevent motion and can stroke up to 155 mm (6.125 in).

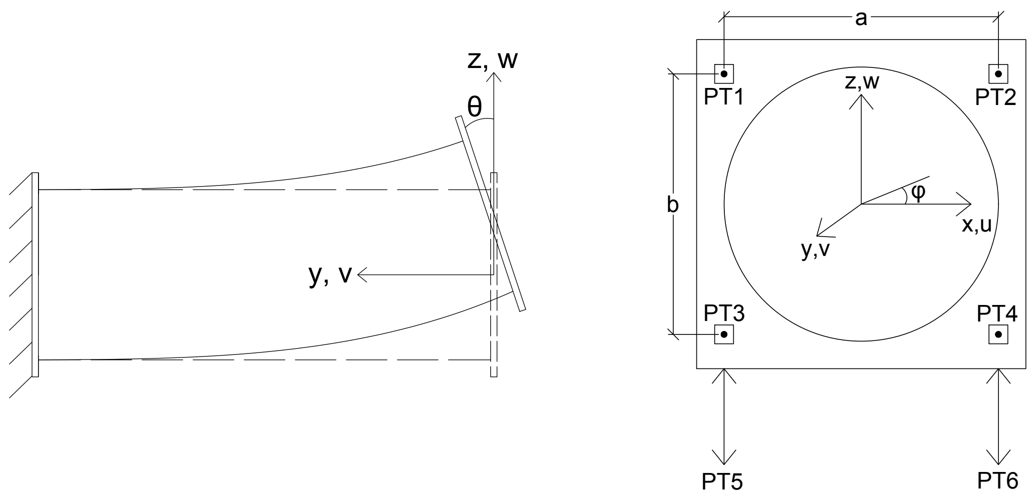

Fig. 10. Coordinate system and PT locations

Experimental Procedure

To conduct a test, the tube and the steel angle on the load arm need to be installed in the correct location for a given T/M load combination. All controls and data collection are completed through custom LabVIEW programming. LabVIEW is used to control the actuator’s stroke in a PID loop and is utilized so that the actuator’s top clevis can be attached to the top ball joint using a shoulder bolt. The actuator is then moved in fine control, increasing or decreasing the stroke, such that the load reading is zeroed. Then the tube is loaded by extending the stroke at 0.025 mm/second (0.001 inch/second), pushing up on the load arm. Testing continues until the actuator displacement is approximately 2 times the displacement at failure (peak load). Unloading occurs at a rate of 0.25

mm/second (0.01 inch/second) until the load reading returned to zero. The load and readings from the six PTs were continuously recorded. These data were used to determine the inward displacement *v*, upward displacement *w*, in-plane rotation *φ*, and out-of-plane rotation θ of the end plate of the test tube specimen using Eqs. 1-4 respectively,

$$v = \frac{\delta_1 + \delta_2 + \delta_3 + \delta_4}{4} \tag{1}$$

$$w = \frac{\delta_5 + \delta_6}{2} \tag{2}$$

$$\theta = \frac{\frac{\delta_1 + \delta_2}{2} - \frac{\delta_3 + \delta_4}{2}}{b} \tag{3}$$

$$\phi = \frac{\delta_6 - \delta_5}{a} \tag{4}$$

where δ_1 through δ_6 represent PT1 through PT6 displacements.

Test Results

This section provides a comprehensive overview of the key results obtained from the experiments, including the failure modes and load-deformation histories. Table 1 provides nominal tube dimensions and the test matrix. Three tubes were tested for each tube size and T/M combination. Self-weight of the tube, end plates, and load arm were taken into account (removed) for these results. Test results are compared with predictions from von Mises yield criterion and Eurocode-based calculations in the subsequent section.

250mm Results

Fig. 11 provides photos of the 250mm tubes immediately after reaching peak load. The 250mm tubes have a D/t of 320 and were the most slender tubes tested. The fixed end of each tube is attached to the reaction beam, which is located at the bottom of each photo. The free end of each tube is attached to the load arm, which is at the top of each photo. The failure modes for bending only are different from failure modes with torsion present. In bending only, the tubes buckle with relatively short half waves around a cross section at failure near the reaction beam end, which had the highest moment. If there is any torsion, buckling waves form over a significant length of the section and at an angle around the tube.

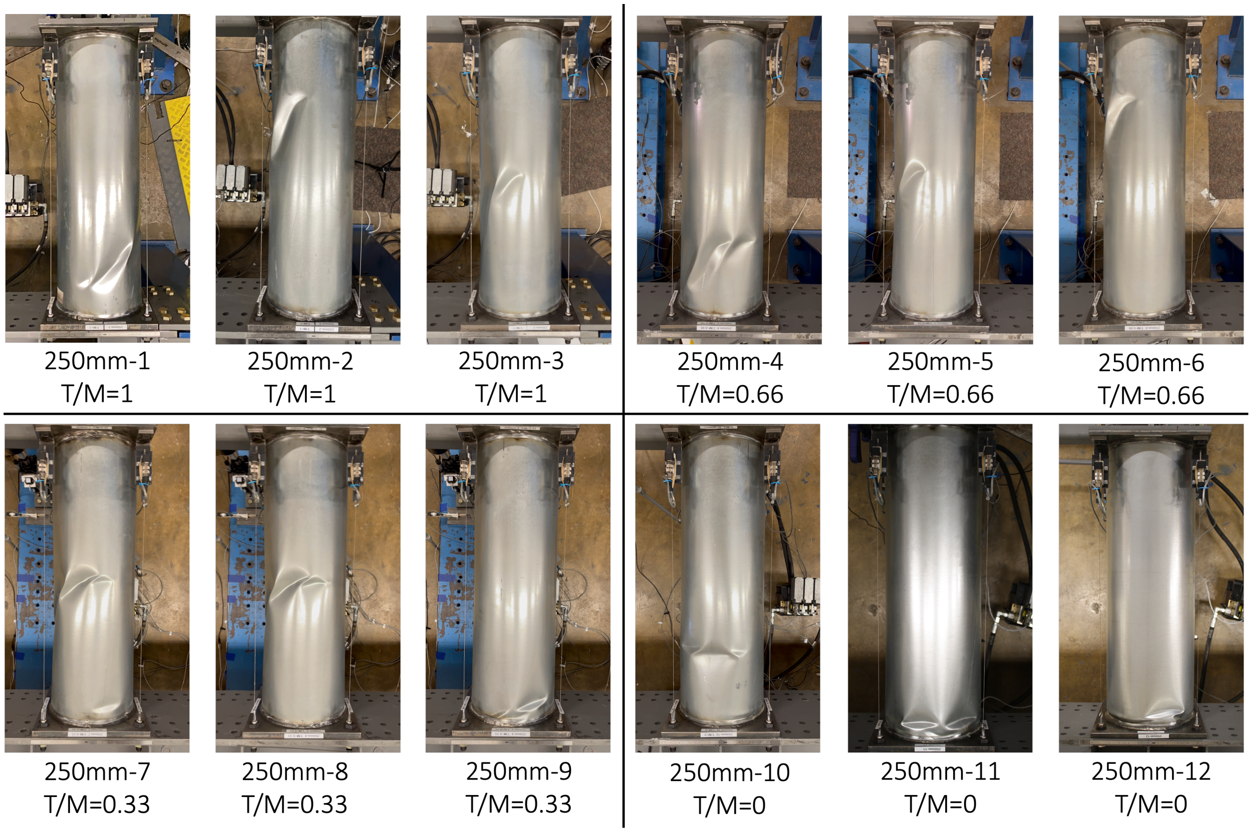

Fig. 11. Photos of buckled 250mm tubes

Fig. 12 provides load vs *w*, or upward plate displacement, of all 250mm tubes. Buckling typically occurred without prior indication for all tubes and usually produced a loud popping sound from the tube. The load-deformation response pattern is the same for each tube, except for 250mm-12, T/M=0, which was the first tube tested – though ultimate load is accurate for this specimen. The rig tie downs to the floor were not fully tensioned for the 250mm and 200mm tubes, causing an irregular initial response and introducing additional measured displacement. This initial deviation in the response was corrected by extrapolating the elastic linear region of the load-deformation curves. The tie downs were fully tensioned for the 150mm and 100mm tubes. As expected, tubes tested in bending only (T/M=0) had the highest failure load. As more torsion (eccentricity in the load arm) is added, failure load decreases. Figs. 13 and 14 provide moment vs θ and torque vs ϕ of the data plotted until peak load, along with the theoretical bending stiffness and torsional stiffness for comparison, where E is the elastic modulus and assumed to be 210 MPa for all tubes, I is the moment of inertia, G is the shear modulus, and J is the polar moment of inertia. The theoretical bending stiffness is greater than the measured bending stiffness, which suggests some additional accommodations are still present in the test. However, the theoretical torsional stiffness matches well with the tests.

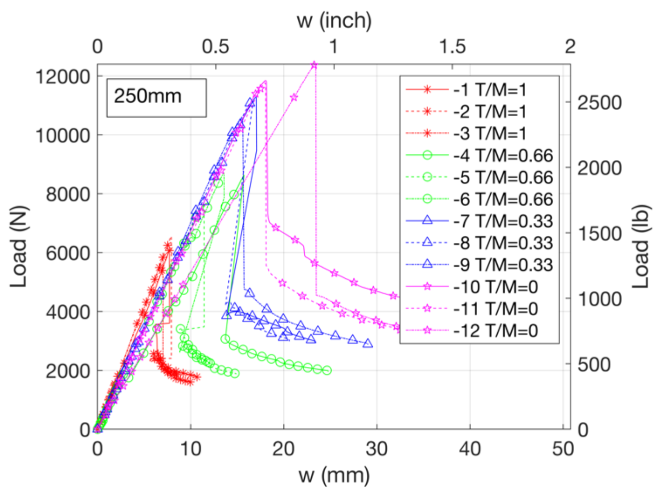

Fig. 12. Load vs w for 250mm tubes

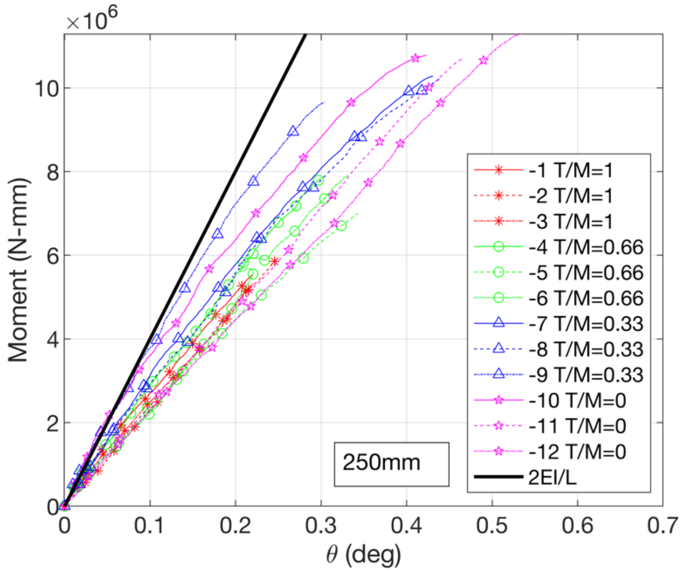

Fig. 13. Moment vs θ for 250mm tubes

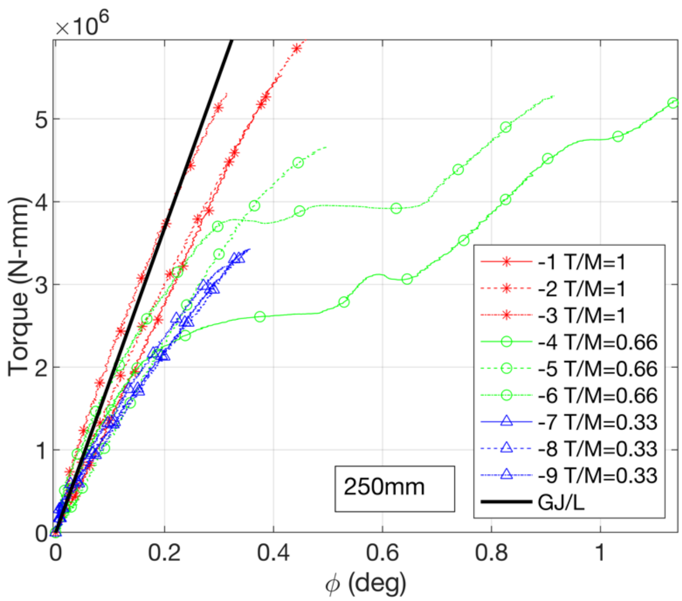

Fig. 14. Torque vs ϕ for 250mm tubes

<u>*200mm Results*</u>

Fig. 15 provides photos of the 200mm diameter tubes after failure. The 200mm tubes have a D/t of 256. These tubes behaved similarly to the 250mm tubes. Like the 250mm tubes, the buckling shapes of the 200mm tubes under bending only (T/M=0) are different from tubes with any torsion. However, not all the 200mm tubes produced a loud popping sound.

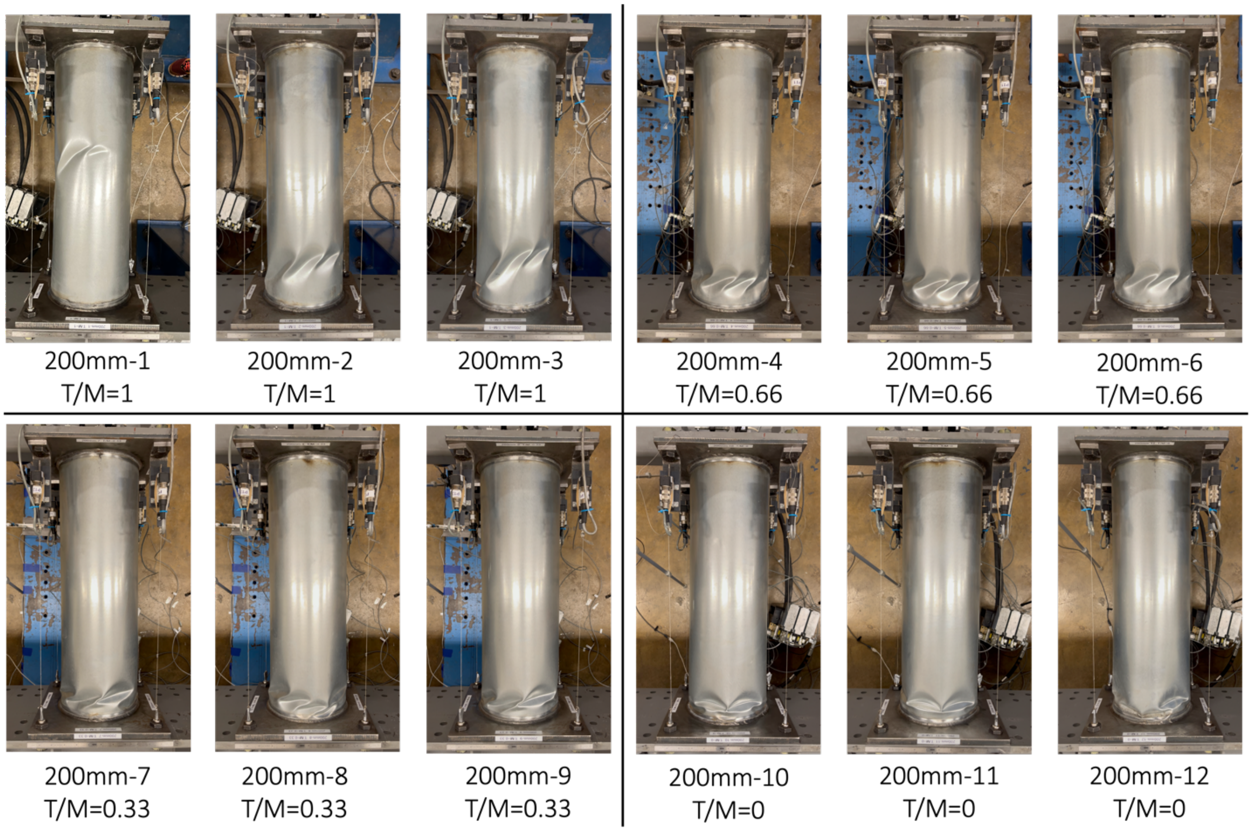

Fig. 15. Photos of buckled 200mm tubes

Figs. 16-18 provide results of the 200mm diameter tubes. Fig. 16 shows load vs displacement of the 200mm tubes. Like the 250mm tubes, buckling of the 200mm tubes occurred abruptly, but the drops in resistance after bucking are smaller than for the 250mm tubes. Again, tubes tested in bending only had the highest failure loads, with failure load decreasing as more torsion is added. The moment vs θ curves and torque vs ϕ curves for the 200mm tubes are depicted in Figs. 17 and 18, respectively. Like the 250mm tubes, the theoretical bending stiffness for the 200mm tubes is greater than the measured bending stiffnesses, while the theoretical torsional stiffness matches well with the tests.

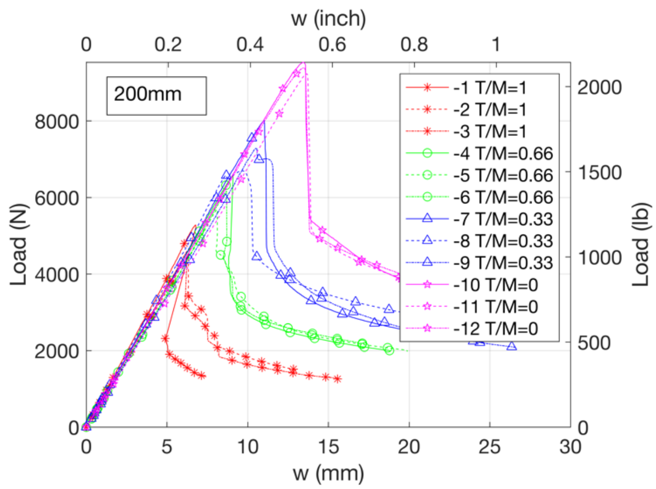

Fig. 16. Load vs w for 200mm tubes

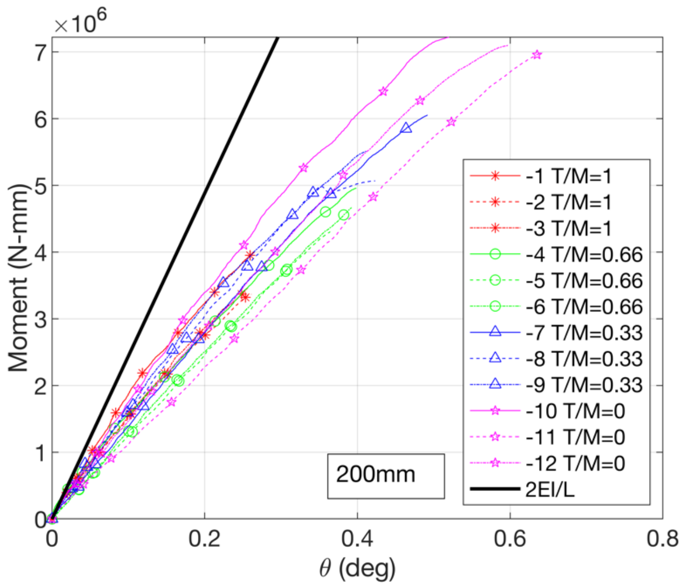

Fig. 17. Moment vs θ for 200mm tubes

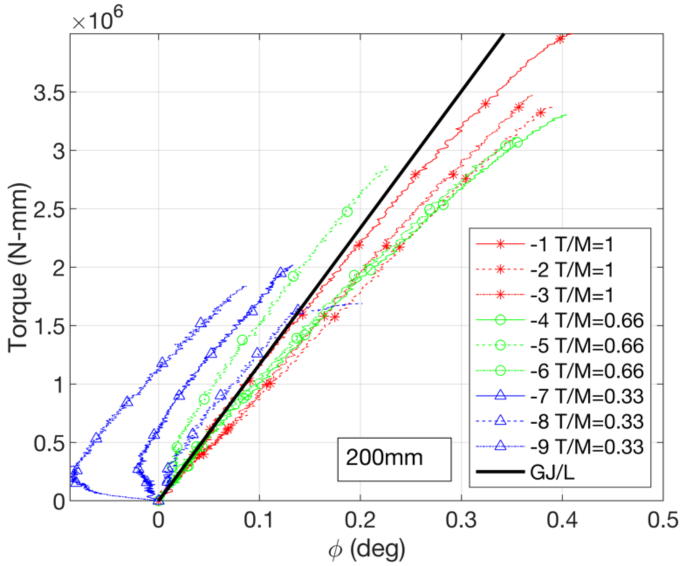

Fig. 18. Torque vs ϕ for 200mm tubes

150mm Results

Fig. 19 provides photos of the 150mm diameter tubes after failure. The 150mm tubes have a D/t of 191. One tube, 150mm-12, is excluded due an accidental stroke out of the actuator. Some of these tubes, specifically tubes 150mm-7, -9, and -11, have failure modes that were not observed in the larger tubes, where only one circumferential wave formed around a cross section near the fixed end.

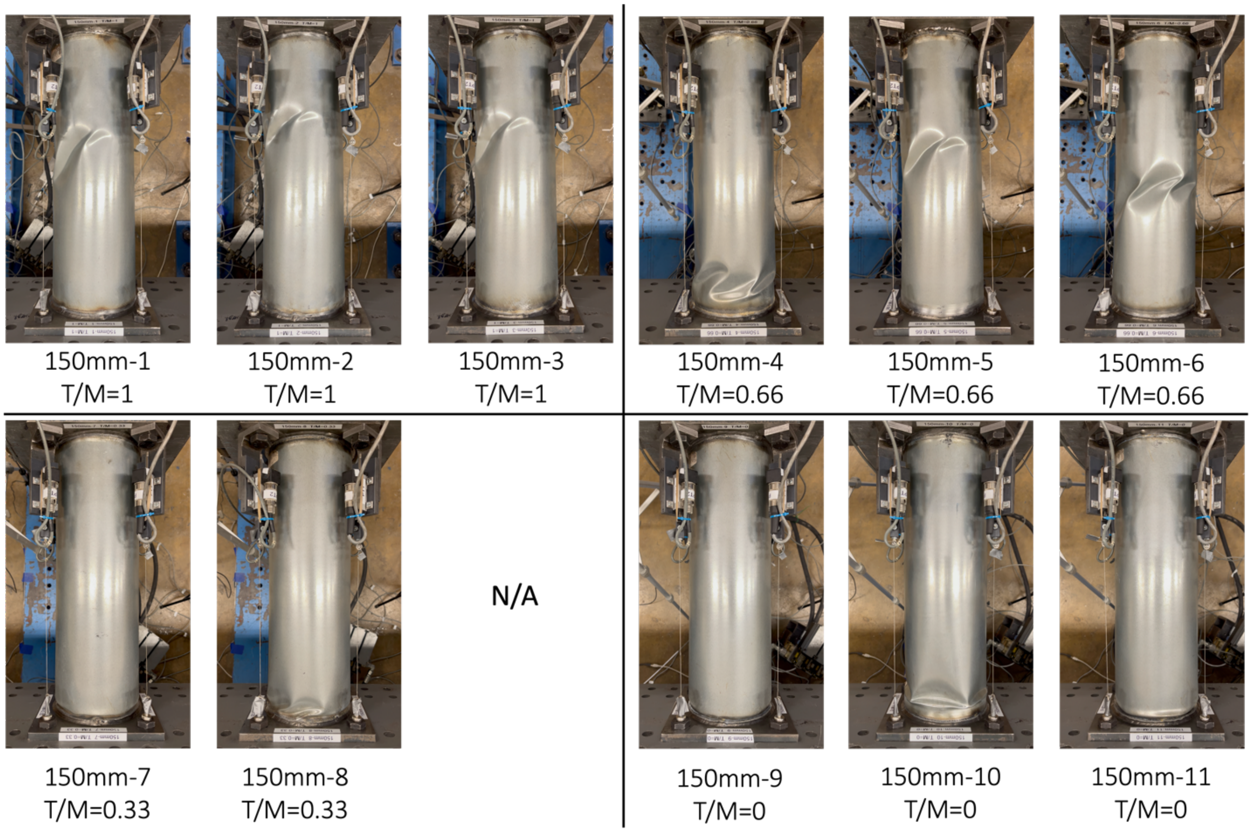

Fig. 19. Photos of buckled 150mm tubes

Figs. 20-22 provide the load vs displacement curves, moment vs θ curves, and torque vs ϕ curves of the 150mm tubes, respectively. In Fig. 20, the response softens shortly before buckling, providing some small warning before failure. However, the drops in load at failure remain substantial. As shown in Figs. 21 and 22, the theoretical bending and torsional stiffnesses match well with the tests.

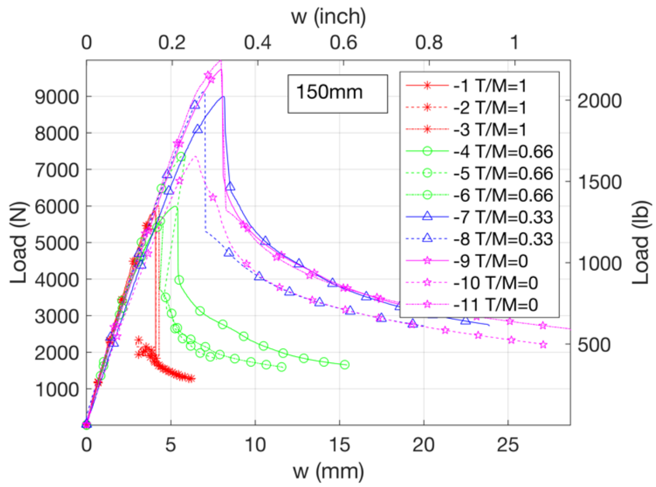

Fig. 20. Load vs w for 150mm tubes

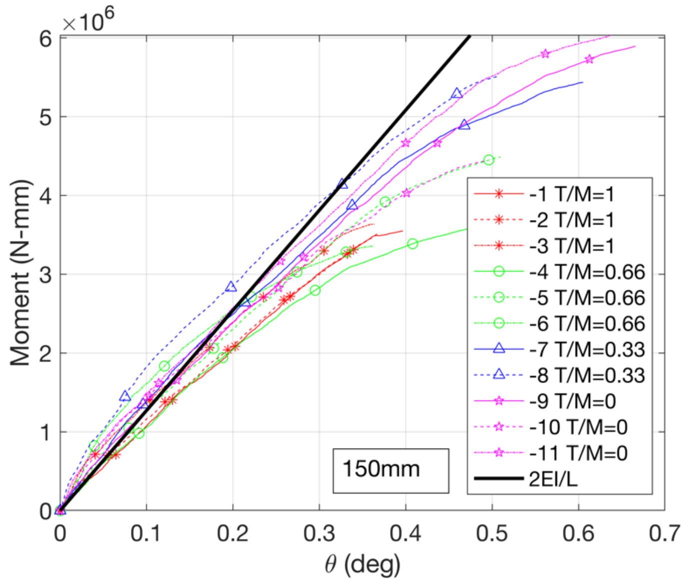

Fig. 21. Moment vs θ for 150mm tubes

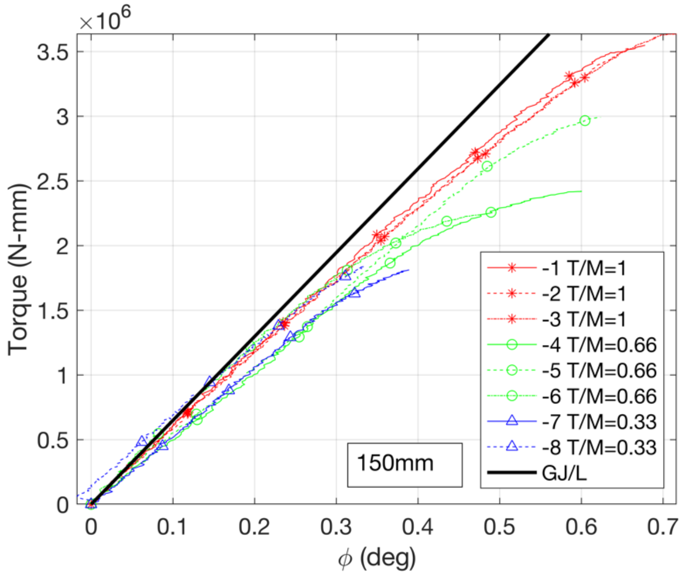

Fig. 22. Torque vs ϕ for 150mm tubes

100mm Results

Fig. 23 provides photos of all 100mm diameter tubes after failure. These are the stockiest tubes tested, with a D/t of 127. The 100mm tubes usually failed with one buckling wave: a circumferential wave for tubes in bending only and waves at different angles for tubes subjected to combined bending and torsion.

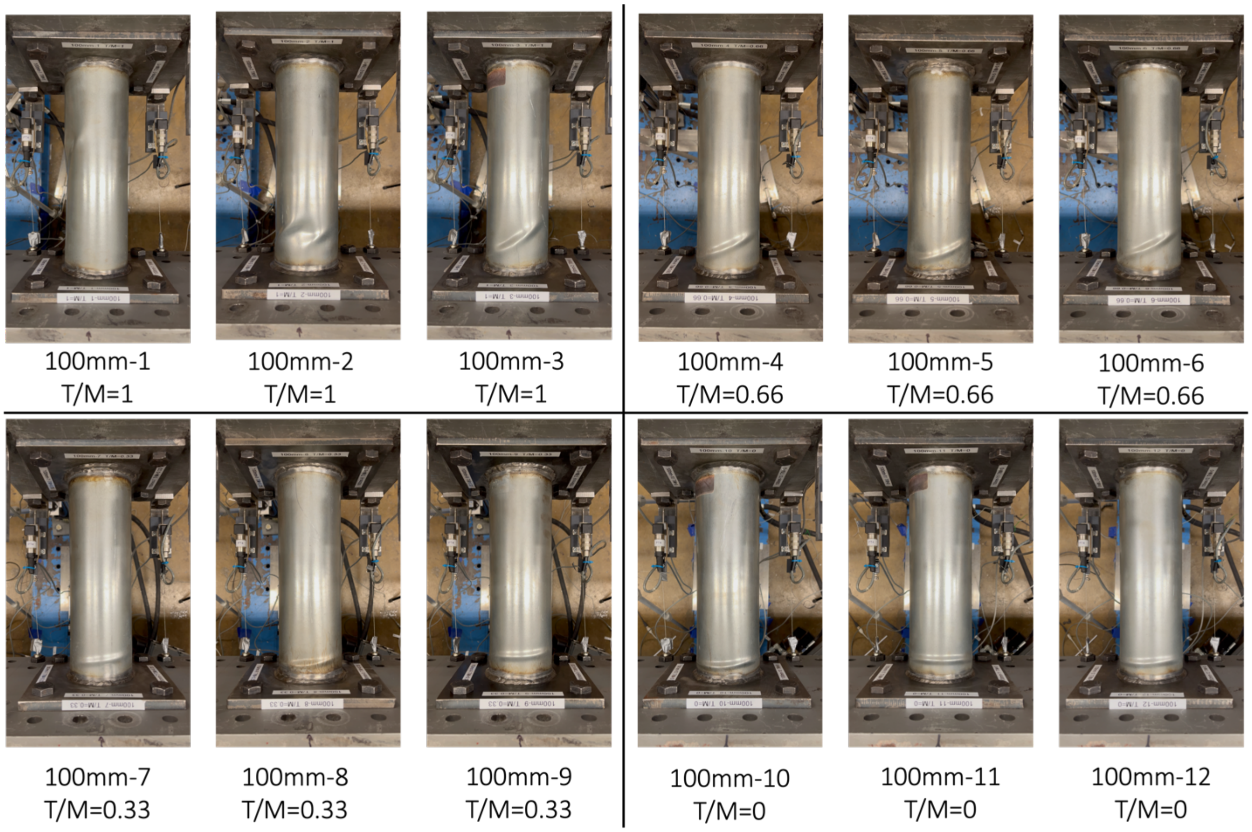

Fig. 23. Photos of buckled 100mm tubes

Figs. 24-26 provide the load vs displacement curves, moment vs θ curves, and torque vs ϕ curves of the 100mm tubes, respectively. As shown in Fig. 24, load drops slowly after reaching peak load, as opposed to the sudden drops observed in the larger more slender tubes. Failure occurs more slowly as D/t ratio decreases. As shown in Figs. 25 and 26, the theoretical bending and torsional stiffnesses match well with the tests.

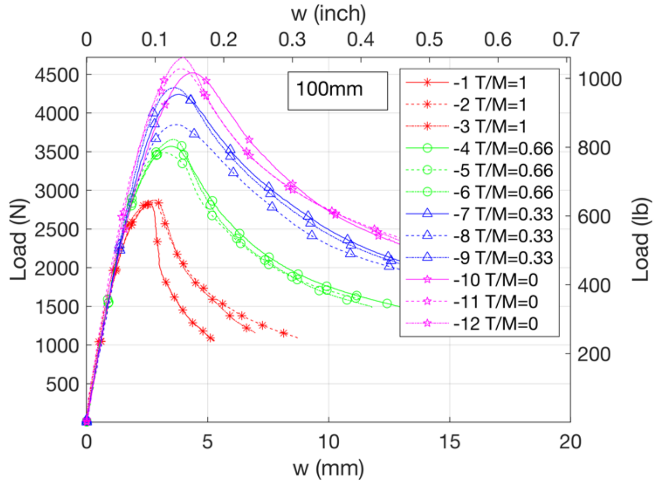

Fig. 24. Load vs w for 100mm tubes

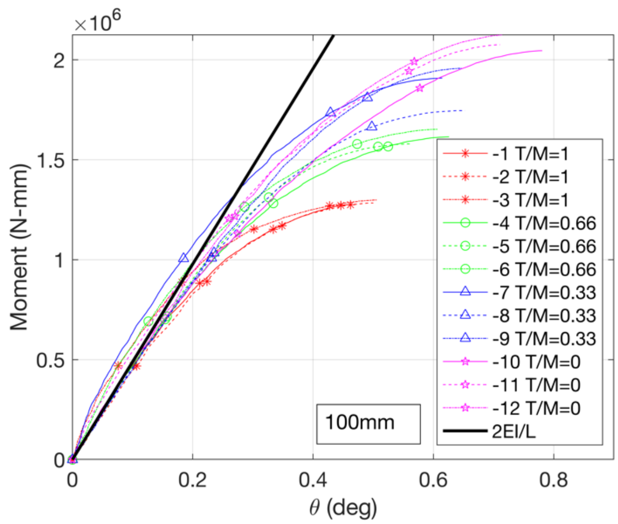

Fig. 25. Moment vs θ for 100mm tubes

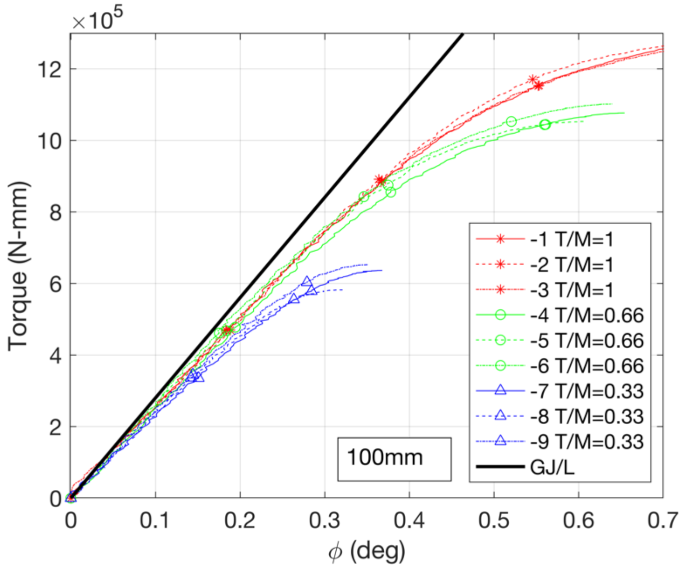

Fig. 26. Torque vs ϕ for 100mm tubes

Table 4 summarizes each tube's maximum torque and bending moment (located at failure). Three tubes were tested for each tube size and T/M combination.

Table 4. Summary of maximum torque and bending moment

		M_{max} (N-mm)			T_{max} (N-mm)		
Tube Size	T/M Ratio	Test 1	Test 2	Test 3	Test 1	Test 2	Test 3
250mm	1	5.530E+06	5.960E+06	5.317E+06	5.529E+06	5.960E+06	5.317E+06
	0.66	7.848E+06	6.992E+06	7.919E+06	5.232E+06	4.661E+06	5.279E+06
	0.33	1.029E+07	1.023E+07	9.657E+06	3.429E+06	3.411E+06	3.219E+06
	0	1.079E+07	1.129E+07	1.129E+07	0	0	0
200mm	1	4.002E+06	3.373E+06	3.482E+06	4.002E+06	3.373E+06	3.482E+06
	0.66	4.965E+06	4.309E+06	4.677E+06	3.310E+06	2.873E+06	3.118E+06
	0.33	6.062E+06	5.071E+06	5.516E+06	2.021E+06	1.690E+06	1.838E+06
	0	7.226E+06	6.998E+06	7.104E+06	0	0	0
150mm	1	3.553E+06	3.525E+06	3.636E+06	3.552E+06	3.525E+06	3.635E+06
	0.66	3.631E+06	4.488E+06	3.356E+06	2.421E+06	2.992E+06	2.237E+06
	0.33	5.439E+06	5.517E+06	N/A	1.813E+06	1.839E+06	N/A
	0	5.901E+06	4.437E+06	6.041E+06	0	0	0
100mm	1	1.276E+06	1.284E+06	1.299E+06	1.276E+06	1.284E+06	1.299E+06
	0.66	1.615E+06	1.580E+06	1.653E+06	1.077E+06	1.053E+06	1.102E+06
	0.33	1.909E+06	1.746E+06	1.958E+06	6.364E+05	5.821E+05	6.527E+05
	0	2.047E+06	2.076E+06	2.127E+06	0	0	0

Strength comparisons and Eurocode-based calculations for combined bending and torsion

von Mises yield criterion

A simplified form of the von Mises yield criterion considering only torsion and bending is provided in Eq. 5,

$$\sigma_b^2 + 3\tau_T^2 = F_y^2 \tag{5}$$

where σ_b is bending stress, τ_T is torsional shear stress and F_y is yield stress. After converting from stresses to actions (assuming bending moment and torsion only) using yield failure criteria for torsion and bending, one arrives at the simplified interaction expression of Eq. 6,

$$\left(\frac{M}{M_y}\right)^2 + \left(\frac{T}{T_y}\right)^2 = 1 \tag{6}$$

where M is moment demand, T is torque demand, M_y is yield moment, and T_y is yield torque. The test results were compared with this simplified von Mises yield criterion as a baseline for comparison.

Eurocode-based calculation

To have a preliminary knowledge on how the test results compare to code-based capacity predictions, we performed calculations using the relevant Eurocode, EN 1993-1-6 (2021). Eurocode provides multiple design approaches for cylindrical shells, including analytical stress-based design, semi-analytical methods such as reference resistance design, and purely computational approaches. The simplest and most commonly employed method is the stress-based design, which uses stress interaction equations. This approach is utilized herein for comparison. The interaction equation for combined loads in Eurocode's format is provided in Eq. 7,

$$\left(\frac{\sigma_{x,Ed}}{\sigma_{x,Rd}}\right)^{k_{ix}} - k_i\left(\frac{\sigma_{x,Ed}}{\sigma_{x,Rd}}\right)\left(\frac{\sigma_{\theta,Ed}}{\sigma_{\theta,Rd}}\right) + \left(\frac{\sigma_{\theta,Ed}}{\sigma_{\theta,Rd}}\right)^{k_{i\theta}} + \left(\frac{\tau_{x\theta,Ed}}{\tau_{x\theta,Rd}}\right)^{k_{i\tau}} \leq 1 \tag{7}$$

where σ_x is axial stress, $\tau_{x\theta}$ is shear stress, σ_θ is hoop stress, subscript Ed means design action, subscript Rd means design resistance, and $k_{ix}, k_i, k_{i\theta}, k_{i\tau}$ are the buckling strength interaction parameters. These interaction parameters for cylindrical shells have been established based on both theoretical and experimental evidence (Rotter and Schmidt 2013). These parameters were derived from simple interactions of basic load cases on cylindrical shells (Yamaki 1984; Schmidt and Winterstetter, 2004). This interaction equation intends to account for elastic buckling of thin shells and generally simplifies to von Mises yield criterion for thick shells. We did not have hoop stress in these tests, so $\sigma_\theta = 0$. Herein, we have assumed σ_x applies to bending moment and not just axial compression. We also assumed the effect of shear force is negligible, as is often true in typical steel design scenarios. The influence of direct shear from bending is negligible for failure loads and only slightly changes failure locations. Therefore, shear stress was calculated only from the direct torque. Nominal strengths were used for comparison, meaning that material factors (partial safety factors) were not considered.

The buckling strength interaction parameters and design resistances can be determined following guidelines outlined in Chapter 9.5 and Annex D of EN 1993-1-6 (2021). Substituting into Eq. 7 results in Eq. 8,

$$\left(\frac{\sigma_{x,Ed}}{\chi_x F_y}\right)^{k_{ix}} + \left(\frac{\tau_{x\theta,Ed}}{\chi_\tau \tau_y}\right)^{k_{i\tau}} \leq 1 \tag{8}$$

where χ_x and χ_τ are strength reduction factors, F_y is tensile yield stress, and τ_y is shear yield stress, where $\tau_y = \frac{1}{\sqrt{3}} F_y$. The demands from testing are $\sigma_{x,Ed}$ and $\tau_{x\theta,Ed}$. Converting the stresses from Eq. 8 into actions yields the interaction expression presented in Eq. 9.

$$\left(\frac{M}{\chi_x M_y}\right)^{k_{ix}} + \left(\frac{T}{\chi_\tau T_y}\right)^{k_{i\tau}} \leq 1 \quad (9)$$

Note, Eurocode's strength reduction factors are dependent on the fabrication quality class, which reflects the severity of geometric imperfections, where class A is excellent quality, class B is high quality, and class C is normal quality.

Comparison of Test Results with Eurocode and von Mises yield Criterion

Figs. 27-30 present interaction diagrams of moment vs torque for each tube size. The markers are located at peak load from the test specimens. For a given tube size and T/M ratio, Eurocode provides three nominal resistance strengths, one for each fabrication quality class (Note that γ_{M1} is set to 1.0 in all comparisons provided herein). The dashed lines represent Eurocode calculations using fabrication quality classes A, B, and C. Solid lines represent the simplified von Mises yield criterion at first yield. Material factors were not considered in these calculations. Most of the test data points fall outside the Eurocode interaction curves, meaning the Eurocode stress-based predictions are generally conservative.

As shown in Fig. 27, the 250mm tubes, which are the most slender tubes, all buckled before yielding. As seen in Fig. 28, the 200mm tubes that were tested only in bending (T/M=0) are above the von Mises curve, implying some inelastic reserve in flexure. 200mm tubes subjected to combined bending and torsion all fall inside the von Mises interaction curve, implying buckling before yielding. As shown in Figs. 29 and 30, the stockier 150mm and 100mm tubes also demonstrate several test points with inelastic reserve in flexure for low T/M ratios.

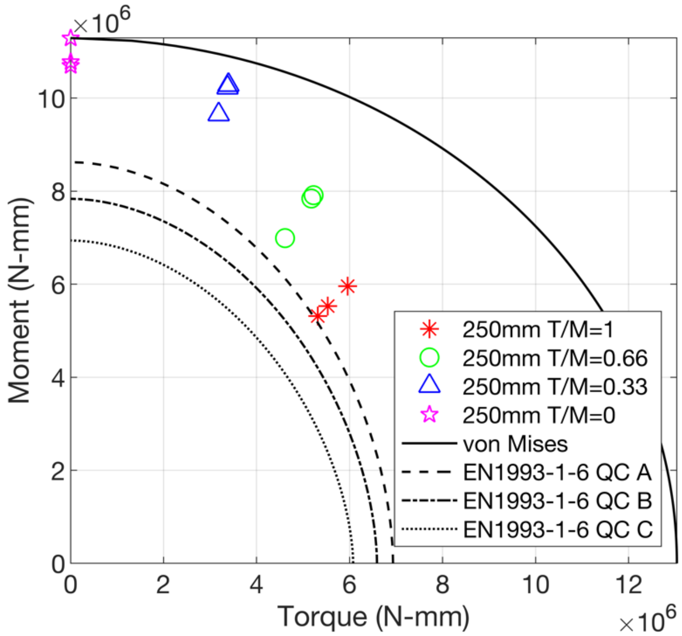

Fig. 27. Comparison of test results with M-T interaction curves for 250mm tubes, D/t = 320

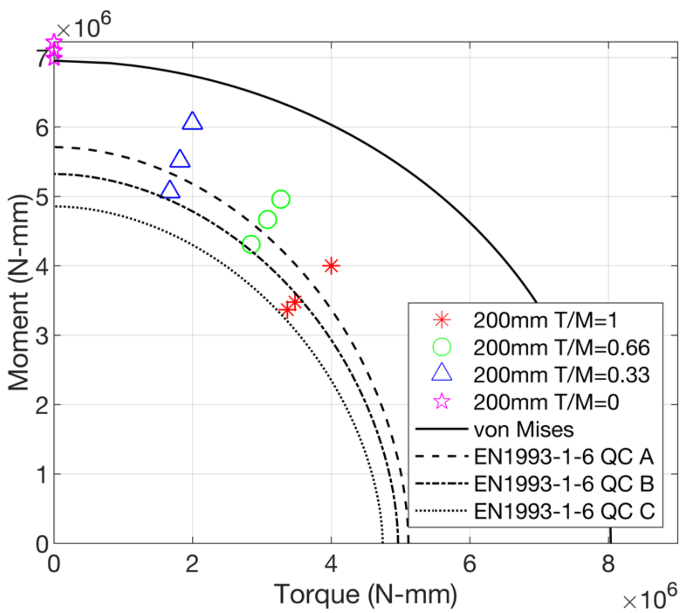

Fig. 28. Comparison of test results with M-T interaction curves for 200mm tubes, D/t = 256

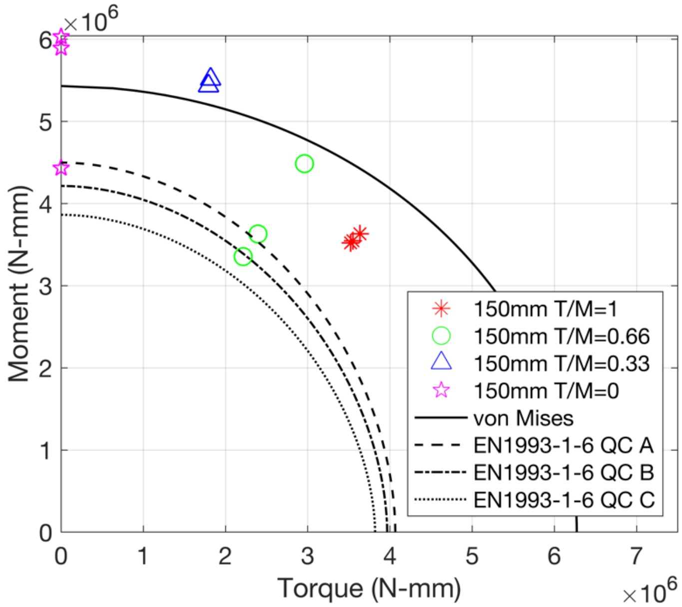

Fig. 29. Comparison of test results with M-T interaction curves for 150mm tubes, D/t = 191

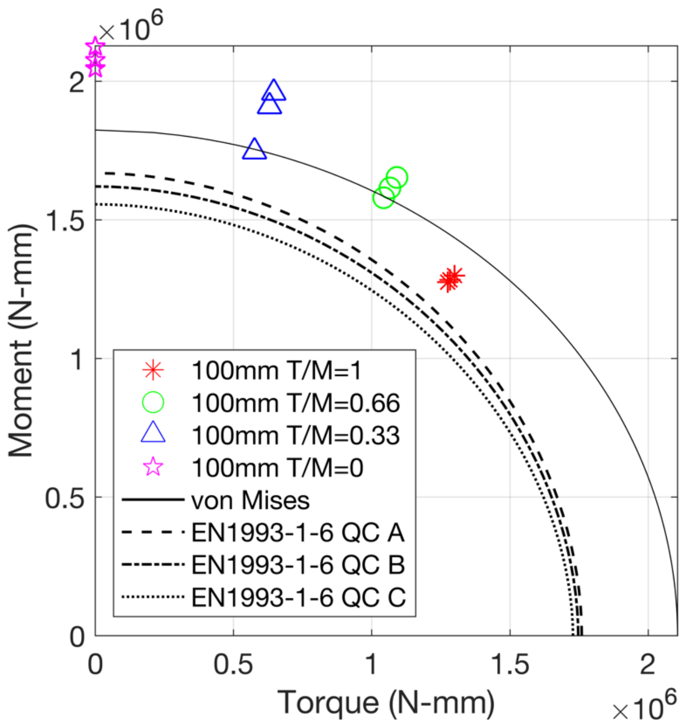

Fig. 30. Comparison of test results with M-T interaction curves for 100mm tubes, D/t = 127

For a given tube size and T/M ratio, Eurocode provides three nominal resistance strengths, one for each fabrication quality class. (Note that γ_{M1} is set to 1.0 in all comparisons provided herein). To compare test-to-predicted performance in the normalized moment-torsion interaction space the radial distance, R, in the space is utilized as defined in Fig. 31.

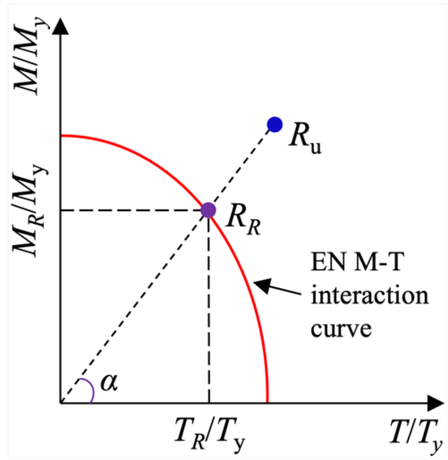

Fig. 31. Definitions of R_u and R_R

For a given quality class, test performance is greater than predicted nominal capacity when $R_u/R_R > 1$. Tables 5 and 6 provide the test-to-predicted ratio statistics by tube size and by loading ratio. According to the experimental results, all tubes fall within classes A-C as defined in EN 1993-1-6. These results show that Eurocode stress-based predictions are conservative for combined moment and torsion, especially when the T/M ratio is low. As T/M decreases from 1 to 0, the mean test-to-predicted ratios increase from 1.08 to 1.24 for class A. On the contrary, there does not appear to be a relationship between the D/t ratio and test-to-predicted ratio. The CV ranges from 0.07 to 0.13, implying relatively low scatter in the test-to-predicted performance.

Table 5. Test-to-predicted ratios by tube size

Tube Specimen		R_u/R_R					
		Class A		Class B		Class C	
Size	D/t	Mean	CV	Mean	CV	Mean	CV
250mm	320	1.20	0.09	1.30	0.09	1.46	0.10
200mm	256	1.07	0.12	1.14	0.12	1.24	0.13
150mm	191	1.20	0.10	1.27	0.10	1.38	0.11
100mm	127	1.16	0.11	1.19	0.07	1.24	0.07
All		1.16	0.10	1.23	0.11	1.33	0.12

Table 6. Test-to-predicted ratios by T/M ratio

T/M Ratio	R_u/R_R					
	Class A		Class B		Class C	
	Mean	CV	Mean	CV	Mean	CV
1	1.08	0.09	1.13	0.09	1.21	0.10
0.66	1.12	0.08	1.18	0.08	1.28	0.10
0.33	1.19	0.10	1.27	0.11	1.38	0.13
0	1.24	0.07	1.33	0.08	1.45	0.09
All	1.16	0.10	1.23	0.11	1.33	0.12

Discussion

The scale model tests provided herein provide initial benchmarks for combined loading, but significant work remains. The initial Eurocode comparisons for the stress-based method show a fair amount of conservatism, but additional comparisons need to be made to fully assess Eurocode's various options; including: consideration of flexural inelastic reserve through the use of reference resistance design (RRD) for bending, application of the generalized linear buckling analysis – material nonlinear analysis (LBA-MNA) method, and evaluation of the use of computational geometric and material nonlinear models with initial imperfections (GMNIA). For all of these methods the evaluation of the geometric imperfections is critical, for the stress-based, RRD, and LBA-MNA the measured scans need to be converted into quality classes, while for the

GMNIA models the measured scans may potentially be utilized directly. Conversion of full-field scan data to discrete classes has unique challenges, which also need to be addressed. Finally, with the modeling protocol established and the performance under combined loads validated, computational models of larger-scale and full-scale cylinders, fabricated consistent with wind turbine support towers, is the natural next step. All the preceding work is underway and will be reported out in the future.

Conclusions

Wind turbine towers are made from thin cylindrical shells, which have high imperfection sensitivity, making predicting their structural response difficult. The combination of bending and torsion at the top of wind turbine towers is often a controlling load case in design that has not seen significant study to date. To address this knowledge gap, an experimental study was completed on 48 cylinders with diameter-to-thickness ratios and bending-to-torsion ratios observed in wind turbine towers. These tests showed that higher diameter-to-thickness ratios result in sudden failures with large drops in load capacity. Adding torsion to bending results in lower load capacities, compared with bending only, and changes the observed buckling and collapse shape in the tube. Eurocode stress-based predictions were fairly conservative for these tests, especially when torsion is low. Future work will involve creating guidelines on how to use laser-scanned data to classify imperfections, as well as establishing high-fidelity finite element models capable of capturing the buckling strength and failure mode of thin-walled cylinders under different loading scenarios, and developing reliable and efficient design approaches for such structural elements.

Data Availability Statement

Some or all data, models, or code that support the findings of this study are available from the corresponding author upon reasonable request.

Acknowledgments

This study is supported by the National Science Foundation under Grant No. 1912481 and No. 1912354. The authors would like to acknowledge Nordfab who donated the specimens, and the project team, including Dr. Michael Shields, Soren Madsen, Dehui Lin, Ziqi Tang, Xi Peng, and Wei Chen who provided comments during various phases of the work. Finally, we would also like to acknowledge Nick Logvinovsky, the lab manager at the Johns Hopkins Thin-Walled Structures Lab, whose assistance was invaluable.

References

AISC (2000). “Load and Resistance Factor Design Specification for Steel Hollow Structural Sections.” Chicago, IL.

ASTM E8/E8M-11. (2012). Standard Test Methods for Tension Testing of Metallic Materials. ASTM International, West Conshohocken, PA. Page 3

Ding, V., Torabian, S., Yun, X., Pervizaj, A., Madsen, S., Schafer, B.W., “Experimental investigation of buckling of thin-walled cylindrical shells subjected to combined bending and torsion.” *Proceedings of the Annual Stability Conference, Structural Stability Research Council*, Charlotte, North Carolina, USA, April 11-14, 2023.

DNV (2002). “Guidelines for Design of Wind Turbines”, 2nd Ed. Det Norske Veritas and Risø National Laboratory.

Donnell, L. H. (1933). “Stability of Thin-Walled Tubes Under Torsion.” National Advisory Committee for Aeronautics. Report No. 479,

ECCS (2021). Eurocode 3: Design of steel structures - Part 1-6: Strength and Stability of Shell Structures.

Felton, L. P. and Dobbs, M. W. (1967). "Optimum design of tubes for bending and torsion." *Journal of the Structural Division*, 93, (4) 185–200.

Jay, A., Myers, A. T., Mirzaie, F., Mahmoud, A., Torabian, S., Smith, E., & Schafer, B. W. (2016). Large-scale bending tests of slender tapered spirally welded steel tubes. *Journal of Structural Engineering*, *142*(12), 04016136.

Jonkman, J. M., and Buhl, M. L. (2005). "FAST user's guide." Golden, CO: National Renewable Energy Laboratory.

Jonkman, J., Butterfield S., Musial, W., Scott, G. (2009). "Definition of a 5-MW Reference Wind Turbine for Offshore System Development." Golden, CO: National Renewable Energy Laboratory.

Gaertner, E., Rinker, J., Sethuraman L., Zahle, F., Anderson, B., Barter, G., Abbas, N., Meng, F., Bortolotti, P., Skrzypinski, W., Scott, G., Feil, R., Bredmose, H., Dykes, K., Shields, M., Allen, C., and Viselli, A. (2020) "Definition of the IEA 15-Megawatt Offshore Reference Wind Turbine." Golden, CO: National Renewable Energy Laboratory.

Nordfab Ducting (2023). https://nordfabductwork.com/.

Ren, W., Zhou, X. H., Gao, Y., Deng, R., Wang, Y. H., & Cao, Y. Q. (2023). Compressive behavior of stiffened steel tubes for wind turbine towers. *Thin-Walled Structures*, *183*, 110372.

Rotter, J. M., Schmidt, H. (2013). Buckling of Steel Shells, European Design Recommendations. ECCS - European Convention for Constructional Steelwork.

Sadowski, A. J., Morata, M. T., Kathirkamanathan, L., Seidel, M., & Rotter, J. M. (2023). On the existing test dataset of isotropic cylindrical metal shells under axial compression and the design of modern metal civil engineering shells. *Structural Safety*, *102*, 102285.

Sadowski, A. J., & Rotter, J. M. (2012). Slender thin cylindrical shells under unsymmetrical strip loads. *Thin-walled structures*, *61*, 169-179.

Schilling, C. G. (1965). “Buckling strength of circular tubes.” *Journal of the Structural Division*, 91 (5) 325–348.

Schmidt, H., Winterstetter, T.A. (2004) "Cylindrical shells under combined loading: axial compression, external pressure and torsional shear", in Buckling of Thin Metal Shells, eds J.G. Teng & J.M. Rotter, Spon, London, pp 261-285.

Seide, P., Weingarten, V.I. (1961). “On the Buckling of Circular Cylindrical Shells Under Pure Bending.” Transactions of the ASME, 112-116.

Teng, J. G., & Rotter, J. M. (1989). Non-symmetric bifurcation of geometrically nonlinear elastic-plastic axisymmetric shells under combined loads including torsion. *Computers & structures*, *32*(2), 453-475.

Timoshenko, S.P., Gere, J. M. (1961). Theory of Elastic Stability. McGraw Hill (reprinted by Dover in 2009), 541 pp.

Wang, J., Fajuyitan O.K., Orabi, A., Rotter, J. M., Sadowski, A. J. (2020) “Cylindrical shells under uniform bending in the framework of Reference Resistance Design.” *Journal of Constructional Steel Research.* Vol 166 105920.

Winterstetter, Th.A., Schmidt, H. (2002) "Stability of circular cylindrical steel shells under combined loading." *Thin-Walled Structures*. Vol. 40 893-909.

Yamaki, N. (1984). Elastic Stability of Circular Cylindrical Shells, North Holland, Elsevier Applied Science Publishers, Amsterdam, 1984.

Yun, X., Gardner, L. (2017). “Stress-strain curves for hot-rolled steels.” *Journal of Constructional Steel Research*, 133, 36-46.

Zhao, X., Tootkaboni, M., Schafer, B.W. (2015). "Development of a Laser-based Geometric Imperfection Measurement Platform with Application to Cold-Formed Steel Construction." *Experimental Mechanics* 55 (9) 1779-1790.